JOURNAL OF SYNCHROTRON RADIATION
ISSN 1600-5775

Three-dimensional characterization of the microstructure in rabbit patella–patellar tendon interface using propagation phase-contrast synchrotron radiation microtomography

Yongchun Zhou,[a,b] Jianzhong Hu,[c,d,e]* Jingyong Zhou,[a,d,e,f] Ziteng Zeng,[a,e] Yong Cao,[c,d,e,f] Zhanwen Wang,[a,d,e,f] Can Chen,[a,d,e,f] Cheng Zheng,[a,e] Huabin Chen[a,d,e,f] and Hongbin Lu[a,d,e,f]*

[a]Department of Sports Medicine, Xiangya Hospital, Central South University, Changsha 410008, People's Republic of China, [b]Department of Orthopedic, Shaanxi Provincial People's Hospital, Xi'an, Shaanxi People's Republic of China, [c]Department of Spine Surgery, Xiangya Hospital, Central South University, Changsha 410008, People's Republic of China, [d]Key Laboratory of Organ Injury, Aging and Regenerative Medicine of Hunan Province, Changsha 410008, People's Republic of China, [e]Research Centre of Sports Medicine, Xiangya Hospital, Central South University, Changsha 410008, People's Republic of China, and [f]Xiangya Hospital, International Chinese Musculeskeletal Research Society Sports Medicine Research Center, Changsha 410008, People's Republic of China.
*Correspondence e-mail: jianzhonghu@hotmail.com, hongbinlu@hotmail.com

Received 23 January 2018
Accepted 22 September 2018

Edited by S. Svensson, Uppsala University, Sweden

Keywords: patella–patellar tendon interface; fibrocartilage layer; PPC-SRμCT; 3D; chondrocytes cell.

Understanding the three-dimensional ultrastructure morphology of tendon-to-bone interface may allow the development of effective therapeutic interventions for enhanced interface healing. This study aims to assess the feasibility of propagation phase-contrast synchrotron radiation microtomography (PPC-SRμCT) for three-dimensional characterization of the microstructure in rabbit patella–patellar tendon interface (PPTI). Based on phase retrieval for PPC-SRμCT imaging, this technique is capable of visualizing the three-dimensional internal architecture of PPTI at a cellular high spatial resolution including bone and tendon, especially the chondrocytes lacuna at the fibrocartilage layer. The features on the PPC-SRμCT image of the PPTI are similar to those of a histological section using Safranin-O staining/fast green staining. The three-dimensional microstructure in the rabbit patella–patellar tendon interface and the spatial distributions of the chondrocytes lacuna and their quantification volumetric data are displayed. Furthermore, a color-coding map differentiating cell lacuna in terms of connecting beads is presented after the chondrocytes cell lacuna was extracted. This provides a more in-depth insight into the microstructure of the PPTI on a new scale, particularly the cell lacuna arrangement at the fibrocartilage layer. PPC-SRμCT techniques provide important complementary information to the conventional histological method for characterizing the microstructure of the PPTI, and may facilitate in investigations of the repair mechanism of the PPTI after injury and in evaluating the efficacy of a different therapy.

1. Introduction

The tendon-to-bone interface (enthesis) has a distinctive three-dimensional (3D) morphology that enables load transfer and minimizes stress concentrations between tendon and bone, which are crucial mechanical components of the skeletal system (Thomopoulos *et al.*, 2006; Deymier *et al.*, 2017; Benjamin & McGonagle, 2009). Unfortunately, this unique tissue that forms at the tendon-to-bone interface is not regenerated during tendon-to-bone healing. Surgical re-attachment of these two dissimilar biological tissues often fails (Thomopoulos *et al.*, 2003). According to reports, the failure rates for rotator cuff injury repair (which requires tendon-to-bone healing) ranges from 20% (small tears) to 94% (massive

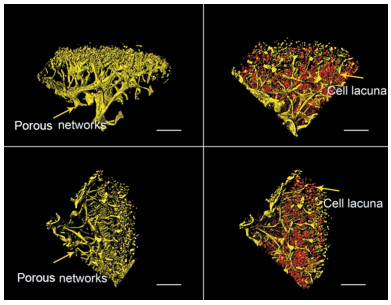

tears) (Harryman *et al.*, 1991; Galatz *et al.*, 2004). The anterior cruciate ligament is the most frequently injured knee ligament; similarly, this complex attachment results in a particularly difficult challenge for effective response to injury, and the outcomes after anterior cruciate ligament reconstruction have been disappointing (Fu *et al.*, 1999). Studies reveal that high failure rates after surgery are due to the poor regeneration ability of the specialized organized tissue that connects tendon to bone (Thomopoulos *et al.*, 2010). In order to develop effective therapeutic interventions for enhanced interface healing, we firstly need to understand the morphology of the enthesis between tendon and bone at the natural physiological status.

The bone–tendon interface has a unique transitional structure with region-specific distributions in cell type and matrix composition (Thomopoulos *et al.*, 2010; Schwartz *et al.*, 2015; Benjamin & Ralphs, 1998). This attachment has been extensively investigated and histologically divided into four distinct zones along the longitudinal direction, including bone (I), calcified fibrocartilage (II), uncalcified fibrocartilage (III) and tendon (IV) (Thomopoulos *et al.*, 2003, 2010; Wang *et al.*, 2010; Lu *et al.*, 2006). Zone I consists of bone, which is made up predominantly of mineralized type I collagen (Thomopoulos *et al.*, 2010; Benjamin *et al.*, 2002). Zone II contains mineralized fibrocartilage, type II and X collagen as well as aggrecan. Zone III consist of fibrocartilage which is composed of a mixture of type II and III collagen as well as small amounts of the proteoglycans aggrecan. Zone IV is highly aligned with collagen type I fibers. However, at present, this classification is likely improper and there are no clear boundaries among the different zones (Thomopoulos *et al.*, 2010; Zelzer *et al.*, 2014; Benjamin & Ralphs, 2001). Instead, a gradation transition exists in the tissue composition from tendon to bone. Currently, a wide range of imaging methods have been developed to visualize the morphological ultrastructure and chemical composition of the enthesis. Characterization of the enthesis has been largely investigated using histological methods with serial sectioning (Lu *et al.*, 2016*a*). Fourier transform infrared spectroscopic imaging has been used to analyze a variety of connective tissues including articular cartilage to bone (Khanarian *et al.*, 2014) and ligament-to-bone interfaces (Qu *et al.*, 2017; Spalazzi *et al.*, 2013). These techniques have shown to correlate well with histological methods in two dimensions. Ultimately, there is still a lack of knowledge about the 3D morphology and quantitative understanding of microstructure features of the interface.

Propagation phase-contrast synchrotron radiation microtomography (PPC-SRμCT) has recently been shown to have tremendous potential as an imaging modality for 3D visualization of bone and articular cartilage microstructures in vertebrates (Horng *et al.*, 2014; Cao *et al.*, 2016; Marenzana *et al.*, 2010; Buenzli & Sims, 2015). It may provide 3D images of bio-samples at micrometre resolution as high as 1 μm (Cao *et al.*, 2016). In addition, the spatial distribution of chondrocytes within the extracellular matrix of articular cartilages without metal staining detected by PPC-SRμCT can be used for analysis to obtain quantitative parameters (Sanchez *et al.*, 2013; Zehbe *et al.*, 2010). So far, the feasibility of obtaining quantitative data regarding the 3D microstructural details of the rabbit normal patella–patellar tendon and distinctive arrangements of chondrocyte organization inside the fibrocartilage layer using PPC-SRμCT has not been widely explored. In our previous study, fibrochondrocytes in the rabbit patella–patellar tendon junction have been detected without phase retrieval of the original image. However, this may cause errors or lead to inaccurate quantitative analysis of the chondrocytes (Chen *et al.*, 2015).

In this context, we aim to optimize and establish a standard imaging procedure to use PPC-SRμCT for 3D characterization of the microstructural and distinctive arrangements of chondrocyte lacuna organization inside the fibrocartilage layer of rabbit normal patella–patellar tendon interface. The features of the chondrocyte lacuna were quantitatively analyzed and our findings were compared with results from histological techniques.

2. Methods and materials

2.1. Animals

Animal care and use and all experimental protocols were approved and conducted in compliance with the guidelines established by the Animal Ethics Committee of Central South University, Changsha, China (permit number: 2013-3-13). Eight skeletal mature female New Zealand white rabbits (18 weeks old, weight 3.5 ± 0.1 kg) were used for the study. Rabbits were housed in a temperature-controlled room with free access to food and water and acclimatized for at least seven days before use.

2.2. Sample preparation

Rabbits were deeply anesthetized with 3% sodium pentobarbital (0.8 ml kg^{-1} intravenous injection), and then an anterolateral skin incision was made longitudinally on the right hindlimb knee. After the patella, patellar tendon and tibial tuberosity were exposed, the patella–patellar tendon interface (PPTI) was extracted and post-fixed with 10% formalin buffer at 4°C for 24 h. The PPTI samples were then rinsed by dual evaporated water and dehydrated by sequential immersion in 70%, 85%, 95% and 100% alcohol (each for 12 h), and were finally dried in air before use. The PPTIs were cut into small sizes of approximately 1.4 mm × 1.4 mm, prior to PPC-SRμCT examination. After scanning, the samples were embedded in paraffin for histological studies with Saf-O/fast green staining. Digital images were captured with these modalities and were subsequently compared and analyzed.

2.3. PPC-SRμCT scanning

The PPC-SRμCT experiment was performed at the synchrotron radiation X-ray imaging and biomedical application beamline (BL13W1) of Shanghai Synchrotron Radiation Facility (SSRF) in China. Synchrotron radiation (SR) was generated from the electron storage ring with an extraction energy of 3.5 GeV and an average beam current of 180 mA; a

wiggler was the source of the X-rays at the beamline. The size of the beam was approximately 45 mm (horizontal) × 5 mm (vertical) and a double-crystal monochromator with Si(111) and Si(311) crystals was used to monochromatize the SR X-rays. The monochromated SR had a flux density of about 5.8×10^{10} photons s^{-1} mm^{-2} and the energy resolution was $\Delta E/E = 5 \times 10^{-3}$. The samples were scanned at a photon energy of 15.0 keV. After penetration through the sample, the X-rays were first converted to visible light by a Lu2SiO5:Ce cleaved single-crystal scintillator. The projections were magnified by diffraction-limited microscope optics (4× and 10× magnification) and digitized by a high-resolution 2048 pixel × 2048 pixel CCD (charge-coupled device) camera with a physical pixel size of 7.4 µm (pco.2000, PCO AG, Kelheim, Germany). The effective pixel size was 1.85 µm for 4× magnification and 0.74 µm for 10× magnification, the exposure time was 2.0 s, and the sample-to-detector distance was 30 cm. For each acquisition, 1200 projection images were captured with an angular step size of 0.15° for 180° as the sample stage was rotated by a precise step motor. Flat-field and dark-field images were also collected during each acquisition procedure, in order to correct the electronic noise and variations in the X-ray source brightness.

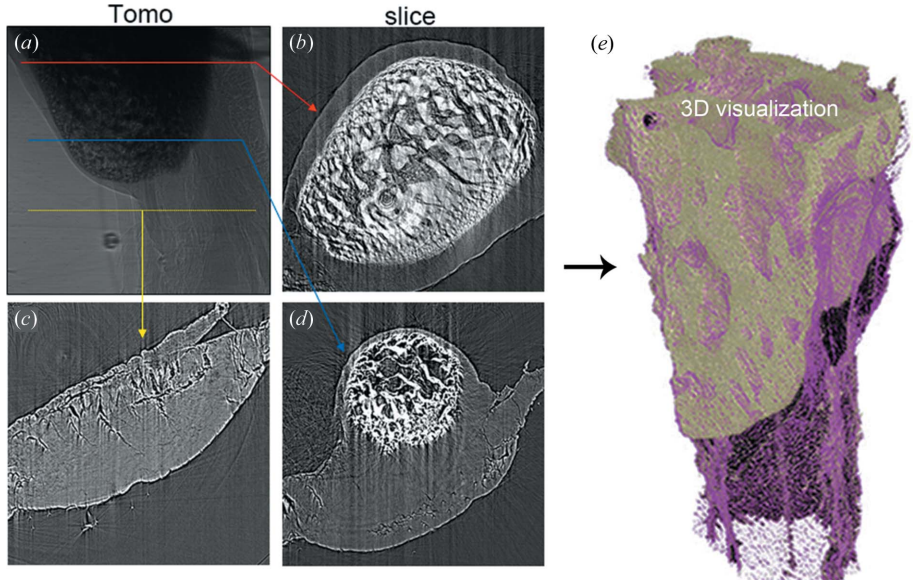

Figure 1
Image reconstruction and 3D visualization process. (*a*) Tomography image of the PPTI. (*b*, *c*, *d*) Two-dimensional slice of the PPTI at different levels of tomography image. (*e*) 3D visualization of the PPTI presented at high resolution.

2.4. Image processing and quantitative analysis

After scanning, projection images of the samples were preprocessed and reconstructed using the software *PITRE* (*Phase-sensitive X-ray Image processing and Tomography Reconstruction*), which was developed at SSRF (Chen *et al.*, 2012). Firstly, extraction of diffraction-enhanced imaging is applied executing phase retrieval for propagation-based phase-contrast tomography. Then phase-contrast enhanced sinogram data were processed using a direct filtered back-projection algorithm (with Shepp–Logan filter). After generation, two-dimensional reconstructed slices of the specimen were truncated and rescaled to a gray value of 0–255 (8 bit gray level). Then, all images of the slices were processed using the commercially available software *Image Pro Analyzer 3D* (Version 7.0, Media Cybernetics, USA) to acquire the full reconstructed 3D images and to obtain quantitative data (Yin *et al.*, 2016) (Fig. 1). From each sample, firstly the boundary of the region of interest (ROI) of the PPTI was selected according to histomorphological characteristics. Secondly, a mask volume including the bone marrow cavity and the chondrocyte lacuna in the PPTI was acquired by using an edge-preserving smoothing bilateral filter and a simple threshold segmentation. The threshold gray value for the segmentation was determined by analysis of the gray-scale histograms and the morphological gradient filter which calculates the difference between the dilation and the erosion of a given image for edge detection. Lastly, the segmentation of the chondrocyte lacuna within the ROI was achieved by setting the thresholds to 106 and 174, respectively. Then, the 3D morphology including diameter, volume and sphericity of the chondrocyte lacuna was obtained.

2.5. Histological observation

To validate the observation by PPC-SRµCT, after scanning, the corresponding specimens were decalcified at room temperature using formic acid, and then dehydrated with graded alcohol series and embedded in paraffin, and cut to 5 µm thickness for morphology staining by Saf-O/fast green. The general characteristics of the PPTI were compared with the PPC-SRµCT imaging data.

2.6. Data analysis

The data are presented as the mean ± standard deviation in this experiment.

3. Results

3.1. Planar X-ray images of PPTI

Fig. 2(*a*) is a physical image of the normal PPTI. After the samples were scanned by SR X-rays, the SR X-ray projection images were obtained (Fig. 2*b*); in these images the patella is displayed in dark gray whereas the patella tendon is shown in bright gray. As shown in Fig. 2(*b*), the interface (red arrow) between the patella and patellar tendon, characterized with a gradual transition zone, was clearly displayed using the SR X-rays. To analyze the imaging capability of SR X-ray radiology, the line profile drawn of the PPTI was recorded and is

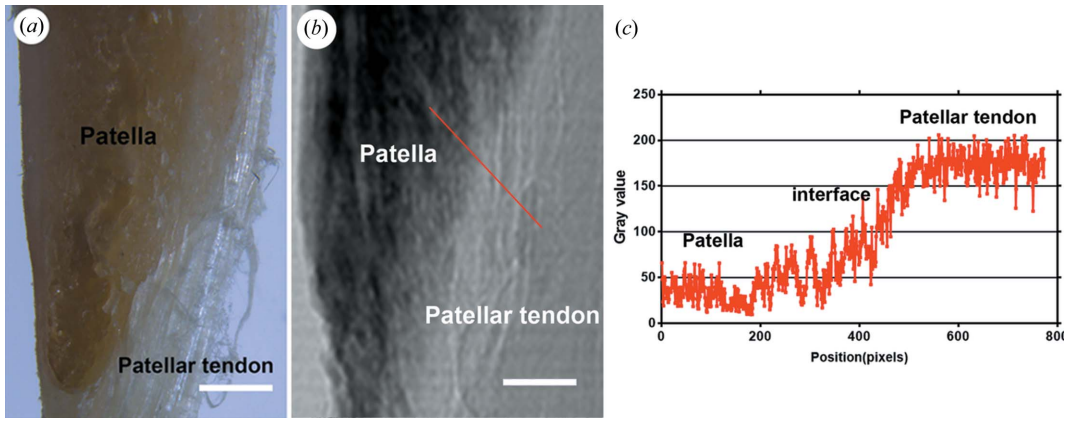

Figure 2
Planar image of the PPTI sample. (*a*). Physical image. (*b*). SR X-ray projection image. (*c*). Line profile displaying the gray value distribution of the PPTI by SR X-ray modality. Scale bar = 800 μm.

presented in Fig. 2(*c*). The gray value in the SR X-ray projection images revealed the PPTI characteristics with gradual transitions in the tissue arrangement. Furthermore, the orientation and anatomical features of the patellar tendon fibers in the SR X-ray projection images are clearly displayed.

3.2. PPC-SRμCT slice imaging and histological analysis of PPTI

After the projection images were obtained, they were reconstructed into two-dimensional tomographic slices. Figs. 3(*a*) and 3(*b*) show the histological section and a magnification image of the PPTI from the same sample, which could serve as a reference for interpretation of the reconstruction results using the PPC-SRμCT technique. Fig. 3(*c*) shows a PPC-SRμCT original slice image of the PPTI, and depicts that the PPTI could be divided into four distinct zones along the longitudinal direction, characterizing its typical morphology: bone (zone I), calcified fibrocartilage (zone II), uncalcified fibrocartilage (zone III) and tendon (zone IV). Figs. 3(*d*) and 3(*e*) are phase-contrast images and 3D color-coding maps, respectively, of the PPCI slice image with PPC-SRμCT, and display a resemblance to the the images with Saf-O/fast green staining and further confirm the PPC-SRμCT

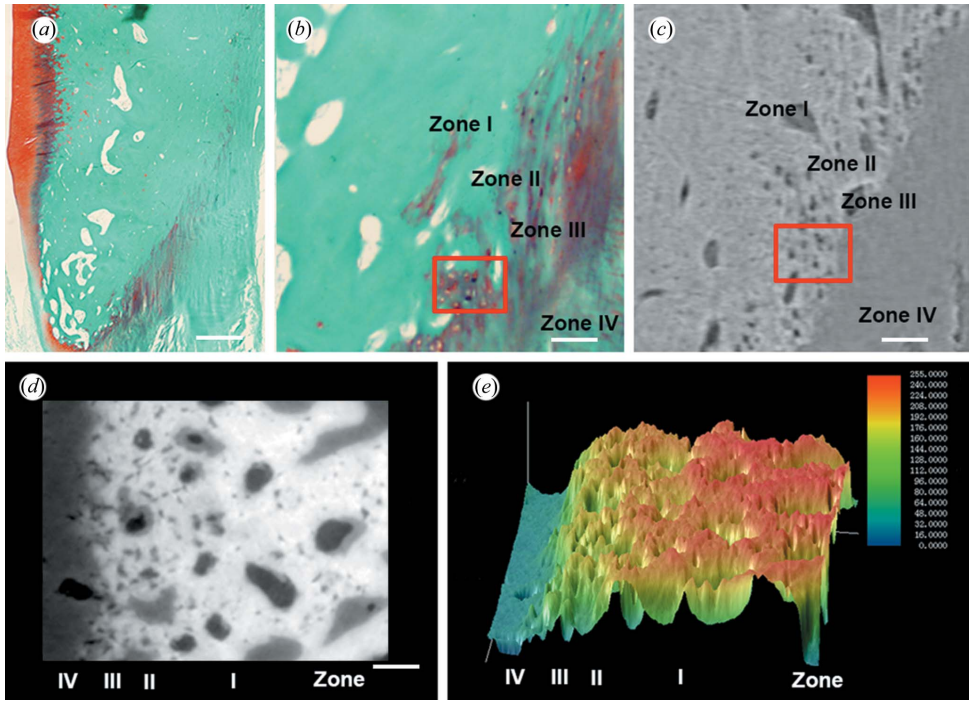

Figure 3
PPC-SRμCT slice imaging and histological section. (*a*) Histological section of the PPTI sample with Saf-O/fast green staining and (*b*) a magnified image. (*c*) Original slice of the PPC-SRμCT reconstruction image. (*d*) Phase-contrast enhancement image of the PPTI. (*e*) 3D color-coding map of the PPCI slice after phase retrieval. The PPTI could be divided into four distinct zones along the longitudinal direction, including bone (zone I), calcified fibrocartilage (zone II), uncalcified fibrocartilage (zone III) and tendon (zone IV). The chondrocyte organization inside the PPTI was marked with a red rectangle. Scale bar = 800 μm (*a*); 200 μm (*b* and *c*); 250 μm (*d*).

findings with the histological method. As shown in Figs. 3(*b*) and 3(*c*), the arrangements of chondrocyte situated inside the lacuna, marked with a red rectangle, which appears to be porous, detected by PPC-SRμCT, matched well with the histological method. However, at present there are no clear boundaries among these four zones; instead a gradation transition exists in the tissue composition from bone to tendon.

3.3. 3D microstructure visualization of the PPTI

PPC-SRμCT preserved the volumetric representation of the PPTI and showed excellent depiction of its complete 3D architecture. As shown in Figs. 4(*a*), 4(*c*), 4(*e*) and 4(*g*), the PPTI is presented with vivid shapes and stereoscopic effects. A distinct zonal pattern (tidemark) between the tendon and bone can be distinguished. After segmentation, the tidemark surface of the PPTI is clearly detectable and rotated to facilitate a clear 3D microstructure visualization (Figs. 4*b*, 4*d* and 4*f*). The 3D inner structure of the tendon is also displayed for the first time (Fig. 4*h*). Furthermore, the lacuna network of the patella is displayed in multi-perspective showing the overall patella structure with the tidemark surface situated at the top and the subchondral bone porous networks starting just below the indicated ROI (Figs. 5*a*, 5*b*, 5*d* and 5*e*). The 3D rendering images of the PPTI were visually screened for cellular structure visualization. A clearly distinguishable cell lacuna with a certain attributed granularity is visible near the tidemark in the 3D image of the PPTI with PPC-SRμCT. The chondrocytes themselves may be situated inside the cell lacuna (Figs. 5*c* and 5*f*).

3.4. Quantitative morphological measurement of the chondrocyte cell lacuna in the PPTI

Figs. 6(*a*) and 6(*b*) show the 3D morphology and spatial distribution, respectively, of the chondrocyte cell resident in the lacuna at the fibrocartilage layer near the tidemark surface of the PPTI. The derived cell lacuna images present the shape and orientation of the chondrocyte inside the fibrocartilage part of the PPTI, forming a catenulate arrangement, and forming a catenulate arrangement along the direction of mechanics. This actually corresponds directly to a typical lacuna in the histomorphology results presented by Saf-O/fast green staining (Figs. 3*a* and 3*b*). A color coding map in terms of connecting beads displays the 3D arrangement pattern of the chondrocyte cell lacuna, presented by single, double and triple connecting beads in the fibrocartilage layer (Figs. 6*c* and 6*d*). The major advantage of the PPC-SRμCT, *i.e.* the preserved integrity and volumetric representation of the PPTI, makes it possible to quantify the morphological structure of the chondrocyte cell lacuna at the PPTI. We measured the mean spheroid diameter of the chondrocyte lacuna, which gave an average maximum and minimum cell length of 9.45 ± 1.216 μm; the corresponding diameter ranged from 8.12 μm to 12.36 μm. The volume of the chondrocyte lacuna in the fibrocartilage zone ranged from 200 μm to 400 μm, with an average volume of 267.38 ± 78.14 μm^3 (Fig. 6*e*). Additionally,

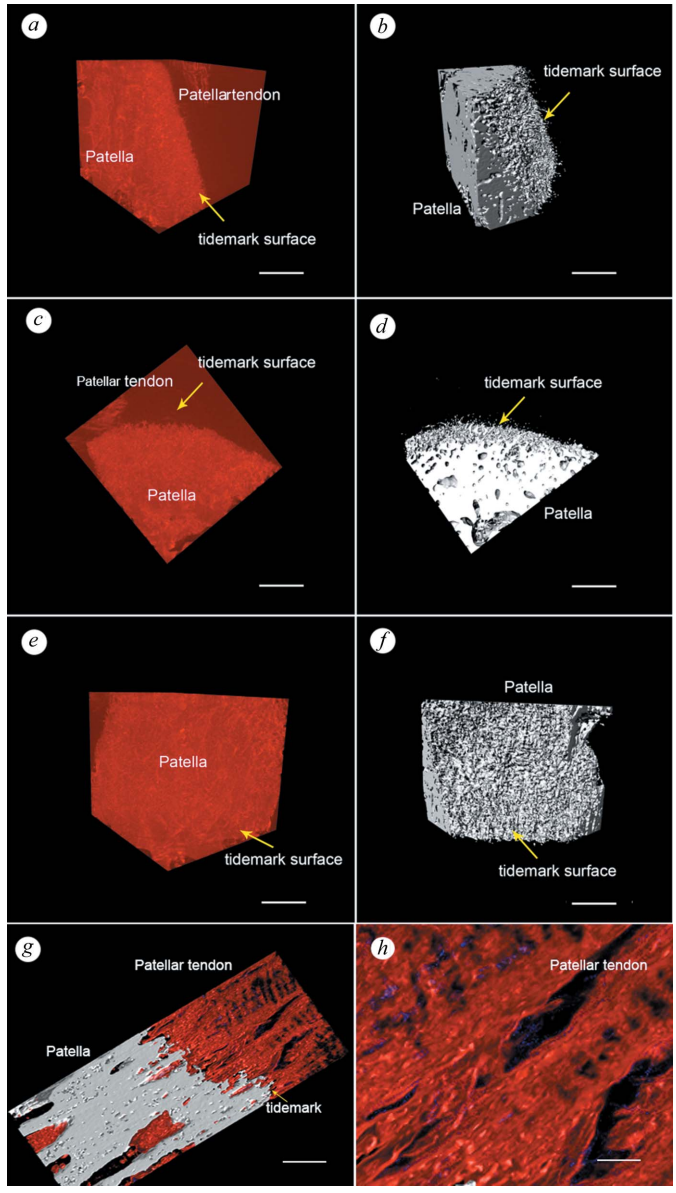

Figure 4
3D microstructure and tidemark surface of the PPTI. (*a*, *c*, *e* and *g*) PPC-SRμCT preserved volumetric representation of the 3D structure of PPTI *via* different perspective including the bone, tendon and interface. (*b*, *d* and *f*) The patella and tidemark surface of PPTI with different perspective. (*h*) The 3D microtructure of tendon. Scale bar = 100 μm (*a*–*g*); 40 μm (*h*).

more than 85.8% of the sphericity ranged from 0.625 to 0.825 and the mean sphericity was 0.721 ± 0.012, indicating that the shape of the chondrocyte lacuna inside the fibrocartilage zone is close to spherical.

4. Discussion

The tendon-to-bone interface occurs across a unique transitional tissue (fibrocartilage) that allows for load transfer and minimizes stress concentrations between tendon and bone (Thomopoulos *et al.*, 2006, 2010). A better understanding of the microstructure of the PPTI in its native state even on a

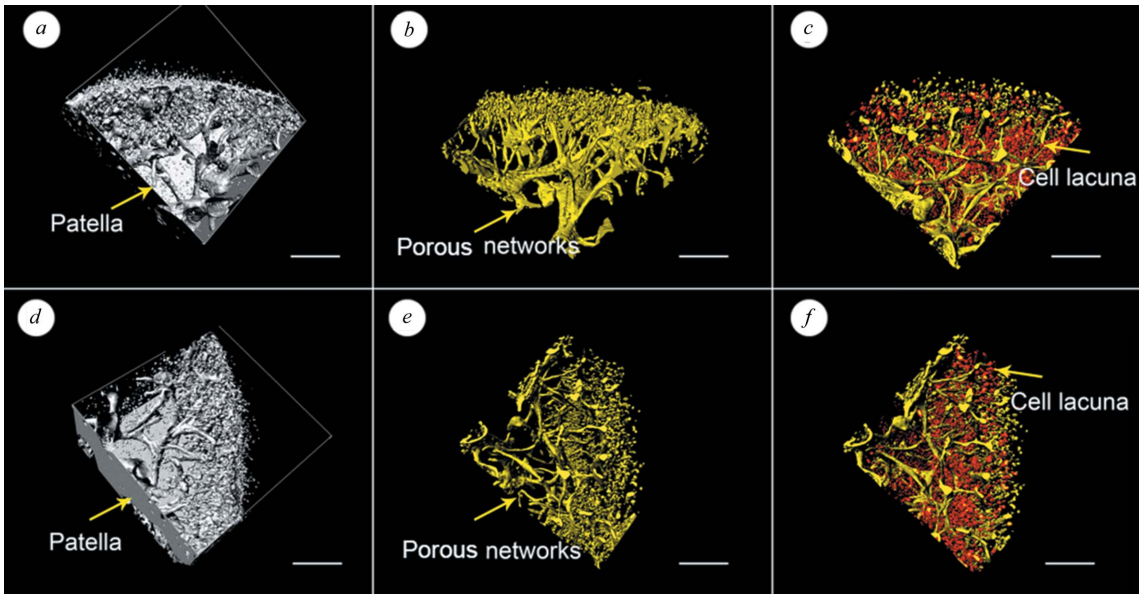

Figure 5
3D porous microstructure networks and cell lacuna near the tidemark of the PPTI. Top and lateral view of the PPTI image (*a* and *d*), porous networks of the PPTI (*b* and *e*), and cell lacuna near the tidemark (*c* and *f*). Scale bar = 100 µm.

single-cell level without destroying the integrity of the tissue may allow researchers to develop a novel therapeutic strategy for enhanced tendon-to-bone healing. Our study demonstrated for the first time that PPC-SRµCT reaches a high cellular spatial resolution that enables volumetric tomographic 3D microstructure of the PPCI, even the 3D morphology of the chondrocytes cell situated inside the lacuna at the fibrocartilage layer of the PPTI. The PPC-SRµCT data further matched well with the image from the histology section with Saf-O/fast green staining, showing similar microstructures in the tomographic slice images with approximately the same image resolution. In addition, the preserved integrity of the tissue makes it is possible to visualize the 3D arrangement of the chondrocytes cell and accurately quantify the volumetric parameters.

In previous studies, the determination of the microstructure of the PPTI in organisms has largely relied on histological sectioning (Lu *et al.*, 2016*a*). Considering the intricate 3D nature of the PPTI, the conventional two-dimensional histological section method is destructive and could not provide sufficient information compared with 3D imaging tools in terms of qualitative and quantitative analysis. PPC-SRµCT is

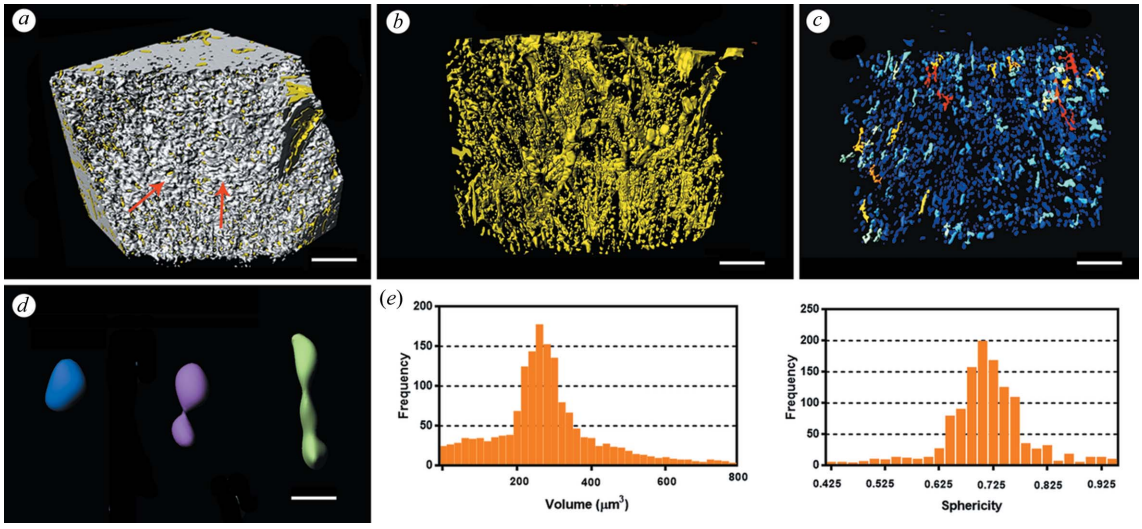

Figure 6
Quantitative morphological measurement of the chondrocyte cell lacuna at the fibrocartilage layer in the PPTI. (*a*) Cell lacuna at the tidemark surface. (*b*) Derived 3D morphology of the chondrocyte cell lacuna. (*c*) Colored maps of the chondrocyte cell lacuna in terms of connectivity of the beads. (*d*) High-magnification 3D images of selective cell lacuna derived at a different area from (*c*); single, double and triple chondrocyte cell lacunae are presented in blue, purple and pale green, respectively. (*e*) Quantitative data of the cell lacuna at the fibrocartilage layer. Scale bar = 100 µm (*a*, *b* and *c*); 10 µm (*d*).

non-destructive, and may not only yield the integrity of the 3D nature of the PPTI but also reveal the volumetric data of the interface (Sanchez *et al.*, 2013). With regard to the anatomy of the PPTI, some of the interest to sports biologists is the ability to visualize the fibrocartilage layer, tissue that is not detectable using conventional X-rays (Zelzer *et al.*, 2014; Sanchez *et al.*, 2013; Lu *et al.*, 2016*b*; Apostolakos *et al.*, 2014). The intrinsic high coherence and brightness of X-rays from a SR facility, coupled with a high-resolution CCD camera, allows the exploitation of the phase-contrast edge enhancement visibility for soft tissue visualization, and provides a tool that has shown great potential for the high-resolution imaging of cartilage (Horng *et al.*, 2014; Cao *et al.*, 2017; Bravin *et al.*, 2013). A demonstration of the phase-contrast methodology based SR for normal human patella cartilage visualization was conducted by Coan *et al.* (2010), and has been subsequently extended for the bone and cartilage interface, and muscle attachment 3D characterization (Sanchez *et al.*, 2013; Li *et al.*, 2014). Zehbe *et al.* (2010) reported that the 3D morphological characterization and the spatial distribution of the cells inside the articular cartilage using SR X-rays exactly matched with results from conventional histology. In our study, we have demonstrated 3D morphological characterization of the PPCI as well as the 3D spatial arrangement of the chondrocytes cell inside the lacuna at the fibrocartilage layer without heavy metal staining using PPC-SRμCT. Furthermore, by surface rendering the 3D shape of the cells inside the lacuna of the PPTI, chondrocyte cell quantification was achieved.

The morphology and distribution of chondrocytes are closely related to the quality of the fibrocartilage, and could be inferred by the function of the fibrocartilage (Schwartz *et al.*, 2015). The PPTI between bone and tendon, which constitutes a complex transition fibrocartilage layer and enables load transfer between structurally and functionally distinct tissue types, is mechanically complex (Thomopoulos *et al.*, 2010). The absence of loading during development impairs fibrocartilage formation between the tendon and bone (Schwartz *et al.*, 2013, 2015; Benjamin & Ralphs, 1998; Thomopoulos *et al.*, 2011). This means that mechanical loading is important and necessary for fibrocartilage formation. We also found that the chondrocyte cells at the fibrocartilage layer have a unique 3D orientation, highly consistent with the direction of the mechanical stress. This could be the structural reason why the stress transfers between the tendon and bone across the fibrocartilage area, and the latter could serve as a functional structure to minimize stress and strain concentrations between tendon and bone. Collectively, PPC-SRμCT provides new insights into PPTI morphology not only at the tissue level but also at the cellular level. Consequently, it will be of interest to make a comparative analysis of the morphology differences of the chondrocyte cell between cartilage and fibrocartilage in a future study.

The PPTI has commonly been categorized into four zones (zone I: bone; zone II: uncalcified fibrous cartilage; zone III: calcified fibrous cartilage; zone IV: tendon fibers) (Benjamin & Ralphs, 1998; Lu *et al.*, 2006; Xu *et al.*, 2014). However, precise 3D anatomical quantitative data of four zones in the PPTI have not been described. In this study, we have proved that PPC-SRμCT has the ability to demonstrate the 3D morphological characteristics of four zones in the PPTI, and is consistent with the location and shape of the histomorphology obtained by conventional histological methods. However, there are no clear boundaries between the four different zone areas (Thomopoulos *et al.*, 2010; Benjamin & Ralphs, 1998). Currently, a wide range of imaging methods have been developed and optimized toward biological imaging at the micro-scale and provide information on the chemical composition both *in vivo* and *vitro*. Fourier transform infrared spectroscopic imaging (FTIR-I) has been used to analyze the chemical composition of articular-to-bone interfaces (Khanarian *et al.*, 2014), and even the matrix composition and organization change across a ligament-to-bone insertion (Spalazzi *et al.*, 2013). They found a continuous change in the tissue structure and composition from tendon to bone and their results are consistence with our findings. These observations demonstrate in-depth insights into composition changes across the soft-tissue region toward bone. As the tendon-to-bone interface is crucial for musculoskeletal functionality, the combination of PPC-SRμCT with FTIR-I for PPTI structure and composition characterization will enhance our understanding of the complexity of the soft-tissue-to-bone interface. From a tissue engineering treatment perspective, combined imaging experiments will guide new scaffold designs and contribute to achieving a biological and functional interface repair between tendon and bone (Olubamiji *et al.*, 2014).

Although our approach offers a number of advantages, there are still some limitations of PPC-SRμCT that should be noted in our current study. In addition to normal PPTI structure analysis, in order to evaluate the effectiveness of interface regeneration strategies, it is meaningful to evaluate the healing response at the interface, as represented in the rabbit animal model evaluated by PPC-SRμCT. Our future study aims to investigate and monitor the 3D morphological change of the interface during the bone–tendon junction healing process. Another limitation is that because of the high resolution of PPC-SRμCT, resulting in a large sample volume, the whole PPTI can only be acquired with low resolution. In this study only a small portion of the PPTI, of size $\sim$1.4 mm $\times$ 1.4 mm, was scanned. Since our study concentrated in particular on establishing a 3D imaging method for attempting to resolve the cellular structure of the PPTI, whole PPTI imaging could only be obtained by sacrificing the imaging resolution.

5. Conclusions

PPC-SRμCT enables a 3D characterization of the microstructure in rabbit patella–patellar tendon interface. Additionally, the 3D morphology of the chondrocyte cell situated inside the lacuna at the fibrocartilage area as well as their quantification were also obtained by this technique. Our findings indicated that SR-μCT is a promising technique, and opens a new dimension in the 3D morphological investigation of microstructure of the PPTI that might be very useful in

studies using animal models to investigate the PPTI repair mechanism after injury and evaluating the therapy efficiency.

Acknowledgements

The authors would like to thank Tiqiao Xiao at the BL13W1 station of the Shanghai Synchrotron Radiation Facility, Shanghai, China, for their kind assistance during the experiments.

Funding information

Funding for this research was provided by: National Key R&D Program (grant No. 2018YFC1105104 to HL); National Natural Science Foundation of China (grant No. 81730068 to HL; grant No. 81472072 to HL); China Postdoctoral Science Foundation (grant No. 2017M622613 to YZ).

References

Apostolakos, J., Durant, T. J., Dwyer, C. R., Russell, R. P., Weinreb, J. H. & Alaee, F. (2014). *Muscles, Ligaments, Tendons J.* **4**, 333–342.
Benjamin, M., Kumai, T., Milz, S., Boszczyk, B. M., Boszczyk, A. A. & Ralphs, J. R. (2002). *Comput. Biochem. Physiol. A*, **133**, 931–945.
Benjamin, M. & McGonagle, D. (2009). *Scand. J. Med. Sci. Sports*, **19**, 520–527.
Benjamin, M. & Ralphs, J. R. (1998). *J. Anat.* **193**, 481–494.
Benjamin, M. & Ralphs, J. R. (2001). *Ital. J. Anat. Embryol.* **106** (Suppl. 1), 151–157.
Bravin, A., Coan, P. & Suortti, P. (2013). *Phys. Med. Biol.* **58**, R1–R35.
Buenzli, P. R. & Sims, N. A. (2015). *Bone*, **75**, 144–150.
Cao, Y., Liao, S., Zeng, H., Ni, S., Tintani, F., Hao, Y., Wang, L., Wu, T., Lu, H., Duan, C. & Hu, J. (2017). *Sci. Rep.* **7**, 43094.
Cao, Y., Zhang, Y., Yin, X., Lu, H., Hu, J. & Duan, C. (2016). *Sci. Rep.* **6**, 21838.
Chen, H. B., Hu, J. Z., Zhou, J. Y., Zheng, C., Wang, Z. W. & Chen, C. (2015). *Nucl. Sci. Tech.* **38**, 110101.
Chen, R.-C., Dreossi, D., Mancini, L., Menk, R., Rigon, L., Xiao, T.-Q. & Longo, R. (2012). *J. Synchrotron Rad.* **19**, 836–845.
Coan, P., Bamberg, F., Diemoz, P. C., Bravin, A., Timpert, K., Mützel, E., Raya, J. G., Adam-Neumair, S., Reiser, M. F. & Glaser, C. (2010). *Invest. Radiol.* **45**, 437–444.
Deymier, A. C., An, Y., Boyle, J. J., Schwartz, A. G., Birman, V., Genin, G. M., Thomopoulos, S. & Barber, A. H. (2017). *Acta Biomater.* **56**, 25–35.
Fu, F. H., Bennett, C. H., Lattermann, C. & Ma, C. B. (1999). *Am. J. Sports Med.* **27**, 821–830.
Galatz, L. M., Ball, C. M., Teefey, S. A., Middleton, W. D. & Yamaguchi, K. (2004). *J. Bone Joint Surg. Am.* **86A**, 219–224.
Harryman, D. T. 2nd, Mack, L. A., Wang, K. Y., Jackins, S. E., Richardson, M. L. & Matsen, F. A. 3rd (1991). *J. Bone Joint Surg. Am.* **73**, 982–989.
Horng, A., Brun, E., Mittone, A., Gasilov, S., Weber, L., Geith, T., Adam-Neumair, S., Auweter, S. D., Bravin, A., Reiser, M. F. & Coan, P. (2014). *Invest. Radiol.* **49**, 627–634.
Khanarian, N. T., Boushell, M. K., Spalazzi, J. P., Pleshko, N., Boskey, A. L. & Lu, H. H. (2014). *J. Bone Miner. Res.* **29**, 2643–2652.
Li, J., Yuan, H., Wu, M., Dong, L., Zhang, L., Shi, H. & Luo, S. (2014). *PLoS One*, **9**, e111939.
Lu, H., Chen, C., Qu, J., Chen, H., Chen, Y., Zheng, C., Wang, Z., Xu, D., Zhou, J., Zhang, T., Qin, L. & Hu, J. (2016). *Am. J. Sports Med.* **44**, 2706–2715.
Lu, H., Liu, F., Chen, H., Chen, C., Qu, J., Xu, D., Zhang, T., Zhou, J. & Hu, J. (2016). *J. Orthop. Res.* **34**, 1697–1706.
Lu, H., Qin, L., Fok, P., Cheung, W., Lee, K., Guo, X., Wong, W. & Leung, K. (2006). *Am. J. Sports Med.* **34**, 1287–1296.
Marenzana, M., Hagen, C. K., Borges, P. D. N., Endrizzi, M., Szafraniec, M. B., Vincent, T. L., Rigon, L., Arfelli, F., Menk, R.-H. & Olivo, A. (2010). *Philos. Trans. R. Soc. A: Math. Phys. Eng. Sci.* **372**, 20130127.
Olubamiji, A. D., Izadifar, Z. & Chen, D. X. (2014). *Tissue Eng. B*, **20**, 503–522.
Qu, D., Subramony, S. D., Boskey, A. L., Pleshko, N., Doty, S. B. & Lu, H. H. (2017). *J. Orthop. Res.* 35, 2513–2523.
Sanchez, S., Dupret, V., Tafforeau, P., Trinajstic, K. M., Ryll, B., Gouttenoire, P. J., Wretman, L., Zylberberg, L., Peyrin, F. & Ahlberg, P. E. (2013). *PLoS One*, **8**, e56992.
Schwartz, A. G., Lipner, J. H., Pasteris, J. D., Genin, G. M. & Thomopoulos, S. (2013). *Bone*, **55**, 44–51.
Schwartz, A. G., Long, F. & Thomopoulos, S. (2015). *Development*, **142**, 196–206.
Spalazzi, J. P., Boskey, A. L., Pleshko, N. & Lu, H. H. (2013). *PLoS One*, **8**, e74349.
Thomopoulos, S., Das, R., Birman, V., Smith, L., Ku, K., Elson, E. L., Pryse, K. M., Marquez, J. P. & Genin, G. M. (2011). *Tissue Eng. A*, **17**, 1039–1053.
Thomopoulos, S., Genin, G. M. & Galatz, L. M. (2010). *J. Musculoskelet. Neuronal Interact.* **10**, 35–45.
Thomopoulos, S., Marquez, J. P., Weinberger, B., Birman, V. & Genin, G. M. (2006). *J. Biomech.* **39**, 1842–1851.
Thomopoulos, S., Williams, G. R. & Soslowsky, L. J. (2003). *J. Biomech. Eng.* **125**, 106–113.
Wang, L., Qin, L., Cheung, W. H., Lu, H. B., Yang, X. H., Leung, K. S., Wong, M. W. & Chan, K. M. (2010). *Br. J. Sports Med.* **44**, 114–120.
Xu, D., Zhang, T., Qu, J., Hu, J. & Lu, H. (2014). *Am. J. Sports Med.* **42**, 2495–2501.
Yin, X. Z., Xiao, T. Q., Nangia, A., Yang, S., Lu, X. L., Li, H. Y., Shao, Q., He, Y., York, P. & Zhang, J. W. (2016). *Sci. Rep.* **6**, 24763.
Zehbe, R., Haibel, A., Riesemeier, H., Gross, U., Kirkpatrick, C. J., Schubert, H. & Brochhausen, C. (2010). *J. R. Soc. Interface*, **7**, 49–59.
Zelzer, E., Blitz, E., Killian, M. L. & Thomopoulos, S. (2014). *Birth Defect Res. C.* **102**, 101–112.